ISSN (Print) 1226-1750
ISSN (Online) 2233-6656
Journal of Magnetics 31(3), 449-464 (2026) https://doi.org/10.4283/JMAG.2026.31.3.449

Flow Dynamics of a Magnetized Ostwald-de-Waele Hybrid Nanofluid with Microorganisms in a Porous Ciliated Channel

Yasir Khan[1], Arshad Riaz[2], Azka Mehreen[2], Safia Akram[3]*, Sami Ullah Khan[4], and A. Alameer[1]

[1]*Department of Mathematics, College of Science, University of Hafr Al-Batin, Hafr Al-Batin 31991, Saudi Arabia*
[2]*Department of Mathematics, Division of Science and Technology, University of Education, Lahore 54770, Pakistan*
[3]*MCS, National University of Sciences and Technology, Islamabad, Pakistan*
[4]*Department of Mathematics, Namal University, Mianwali, Pakistan*

(Received 3 August 2026, Received in final form 17 September 2026, Accepted 21 September 2026)

This study presents a flow model to investigate Ostwald–de-Waele hybrid nanofluid flow under magnetic field effects containing platelet-shaped nanoparticles, with particular emphasis on activation energy and gyrotactic microorganisms. The analysis focuses on bioconvective magnetohydrodynamic (MHD) flow of ciliated bio-nanomaterials through a symmetric channel embedded in a non-Darcy porous medium. Slip boundary conditions are imposed along the channel walls to reflect realistic biological interfaces. The effects of thermal radiation, nanoparticle transport, activation energy and microorganism motility further encourage the thermal, concentration and bioconvective characteristics of the flow. Semi-analytical solutions for velocity, temperature, nanoparticle concentration and motile microorganism profiles are obtained using the Homotopy Perturbation Method (HPM). The results show that ciliary motion and electroosmotic forces significantly influence flow transport and pumping characteristics, while the power-law rheology modifies the shear-dependent flow behavior. These findings provide useful insights into cilia-driven microfluidic transport with potential applications in biomedical and engineering systems.

Keywords : Ostwald-de-Waele hybrid nanofluids, magnetic field, microorganisms, non-Darcy porous channel, thermal radiations

1. Introduction

Cilia comprise fragile structures that imitate threads located in many microscopic creatures. Cilia, which are typically 10 mm long, may readily flex and support a variety of intricate transport systems. In order to carry liquids, food and other substances, cilia are regarded as an integral part of the organism's biosystem. The potential applications of both mobile and immobile filament in many biotic processes have recently attracted the attention of copious researchers in specialized domains like engineering, mathematics and medicine. Using ciliary movement within a curved channel's walls, Arslan *et al.* [1] presented an empirical overview of mixed convectional flow of non-Newtonian Casson fluid. Siddiqui *et al.* [2] worked on an incompressible Newtonian fluid flowing in a channel utilizing MHD, yielded by cilia. The generation of entropy in MHD-driven ciliary Prandtl fluid transport was examined by Munawar *et al.* [3] by applying slips at wall of the channel. According to investigation, cilia lengthening and the slip influence at the boundary can reduce the entropy in the channel. An abstract study of a viscous fluid caused by cilia waves moving metachronally along a curved enclosure regarding the effects of a porous media wad done by Asghar *et al.* [4]. The movement of the cilia has been the subject of numerous recent publications [5-7].

A particle suspended in a fluid of the size of a nanometer is referred to as a nanofluid. Choi [8] first put up the idea of a nanofluid in 1995 in an attempt to speed up the heat transfer. The thermophysical properties of nanofluids are much superior to those of typical base liquids, such as oil or water, like increased viscosity, heat diffusivity and heat conductivity. Sheikholeslami [9] examined the magnetic fields affected thermal transfer and nanofluid dynamics within porous walls. Hussain *et*

©The Korean Magnetics Society. All rights reserved.
*Corresponding author: Tel: +92-300-9825620
E-mail: drssafiaakram@gmail.com
drsafiaakram@mcs.edu.pk (Safia Akram)

© 2026 Journal of Magnetics

al. [10] revealed a multiphase motion of Casson fluid using gold nanoparticles. In an effort to increase thermal conductivity of the base liquid, a new kind of nanofluids recognized as “hybrid nanofluids” has been introduced in literature. Almaneea's research [11] described the hybrid nanomaterials affected mass and thermal transformation in both homogeneous and heterogeneous chemical processes. Shah *et al.* [12] studied the Prandtl hybrid nanofluid flow model numerically. This model considers Darcy-Forchheimer, oblique magnetic field and the impacts of heat radiation over a stretched cylinder. Metal and metal oxide nanoparticles can work together to create a hybrid nanofluid that has improved stability, chemical inertness and excellent heat conductivity [13, 14]. A detailed literature review on nanofluid, MHD and porous media can be cited in the references [15-17].

One type of microbe that moves because of the torque produced by the system's gravitational and viscous forces is the gyrotactic motile microorganism. A novel form of hydromagnetic transport of a nanofluid along a porous, oscillating vertical surface was used to study bioconvection by Mutuku and Makinde [18]. Ahmad *et al.* [19] anticipated that a horizontal plate inserted in a porous medium would contain a motile bacterial bioconvective flow and nanoparticles. According to their findings, the rate at which motile bacteria spread throughout the flow is significantly influenced by the bioconvection characteristics. Recently, research on bioconvection and motile bacteria in porous media have been published in [20, 21].

To initiate a chemical reaction in a system, the least amount of energy required is called activation energy. In binary chemical reactions, it could be useful. Hayat *et al.* [22] talked about the impact of activation energy on rotational non-Darcian three-dimensional nanofluid dynamics. Jagadesh *et al.* [23] claim that the supply of activation energy promotes mass diffusion and controls thermal indulgences. Their discovery could be beneficial for medicine delivery and blood flow control systems. In electromagnetichydrodynamics (EMHD), mutually orthogonal electric and magnetic fields are simultaneously taken into account, along with how they interact with either viscous or inviscid flows. Within a peristaltic flow domain with symmetric walls, Souayeh *et al.* [24] considered the motion of a hybrid nanofluid under a variety of influences, e.g., gyrotactic bacteria, activation energy, electromagnetohydrodynamic and solar radiations. Electroosmosis and thermal radiative heat transmission are analyzed by Prakash *et al.* [25] in relation to the Casson hybrid mixed convection nanofluid in a rotating system that is propelled by an exponentially accelerating plate adjacent to a porous medium. The dynamics of a hybrid nanofluid in a microchannel that is inclined and ciliated, subjected to diverse physical impacts, solar radiation, activation energy, electromagnetohydrodynamics and gyrotactic microbes are investigated by Alfwzan *et al.* [26]. Dolui *et al.* [27] examined heat transfer at nanolayer interfaces and nanoparticle shape effects in EMHD micromagnetorotational ternary nanofluid flow through a diseased bifurcated artery. Xu *et al.* [28] developed a magneto-pneumatic soft actuator with bi-directional torsional motion, demonstrating the potential of magnetic actuation for advanced microfluidic and biomedical systems.

Shear rate and shear stress have a non-linear connection that sets non-Newtonian fluids apart from Newtonian one [29]. Heat transfer becomes more complicated as the dynamic viscosity's flow properties change in response to shear stress. A study of bioconvective non-Newtonian nanofluid flow was presented by Ajithkumar and Lakshminarayana [30]. A Casson nanofluid that produces microorganisms was accounted for to comprehend the flow specimen and porous systems were investigated utilizing the Darcy–Forchheimer law. Various mathematical models, including the power-law model [31], Ree–Eyring model [32], Second-Grade Viscoelastic Fluid [33], third Grade [34], Eyring–Powell [35] and the Casson model [36] are used to describe the non-Newtonian fluid behavior. Ostwald de Waele, another name Power Law model is the most often used of these models since it is straightforward and accurately depicts fluids with a wide, diverse shear rate. A broad category of fluids that exhibit shear-induced thickening and thinning are recognized as power-law fluids. This is an example of a fluid that is not Newtonian and independent of time or a generalized Newtonian fluid. In an exhausted chamber with an inner oval cylinder, Jamshed *et al.* [37] examined the corporal parameters of Ostwald-de Waele nanofluids’ mixed convection in MHD. Currently accessible literature presents related non-Newtonian models as [38–40].

To the best of the authors' understanding, there has been no earlier investigation that has simultaneously analyzed the integrated effects of power-law rheology, gyrotactic microorganism-induced bioconvection, activation energy, electroosmotic forces, magnetic effects and porous resistance on cilia-driven transport of hybrid nanofluids within a symmetric microchannel with slip boundary conditions. The originality of the current research is in the incorporation of these interconnected physical mechanisms into an Ostwald-de Waele fluid model, offering a more thorough elucidation of cilia-driven transport and thermal and mass transfer in microscale systems. Gyrotactic microorganisms and activation energy, in particular, offer

a more accurate depiction of bioconvective and reactive transport processes and the model can take into account significant microfluidic operating conditions thanks to electroosmotic forcing, porous resistance and wall slip. Practical applications including lab-on-a-chip devices, microfluidic pumping and mixing, targeted drug delivery systems, biomedical transport and thermal management of micro-scale devices may benefit from the suggested paradigm. The homotopy perturbation method (HPM) is used to provide semi-analytical solutions for motile microbe distributions, temperature, velocity and nanoparticle concentration. Additionally, streamline patterns, pressure gradient and pressure rise are examined to describe trapping phenomena and pumping performance. Thus, the combined approach offers valuable theoretical understanding of the regulation of non-Newtonian nanofluid movement in biomedical and microfluidic applications.

2. Modeling of the Physical Problem

In the context of gyrotactic microorganism behavior, hybrid nanofluid's flow dynamics in the EMHD ciliated channel are considered, together alongside the impact of thermal radiation and activation energy. The $\check{Y}$-axis is transverse to the inclined ciliated channel, where flow is modeled in the axial direction. Ciliary propulsion initiates the flow and a uniform magnetic field is applied in a transverse orientation. The left wall, with a temperature of T_1 and a concentration of C_1, contrasts with the right wall, which has a temperature of T_0 and a concentration of C_0, as shown in Fig. 1.

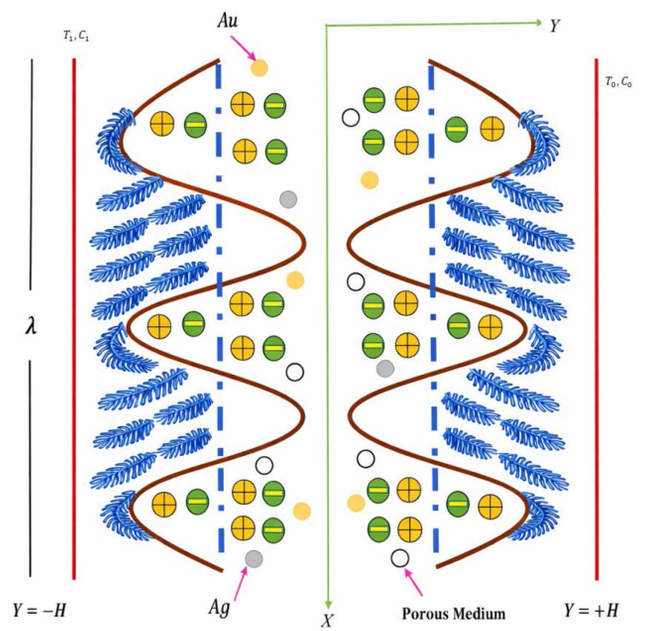


Fig. 1. (Color online) Cilia flow of hybrid nanofluid in porous channel.

An inclined ciliated microchannel can have the following mathematical description [4-6]:

$$\check{Y} = H(\check{X},t) = \pm\left(a + a\varepsilon\cos\left(\frac{2\pi}{\lambda}(\check{X}-ct)\right)\right). \tag{1}$$

where, H indicates the microchannel's wall and a is the mean half-width. The cilia length in relation to a is determined by the non-dimensional parameter ε; $a\varepsilon$ is the metachronal wave's amplitude; c, t and λ correspond to wave velocity, time and wavelength, accordingly.

The parallel poster of ciliary tips can be written as follows:

$$\check{X} = h(\check{X},X_0,t) = X_0 + a\alpha\varepsilon\sin\left(\frac{2\pi}{\lambda}\right)(\check{X}-ct). \tag{2}$$

where X_0 specifies the fluid particles' reference position and α depicts the wave's eccentricity. Cilia's longitudinal and transverse velocities are visible in the following geometries:

$$U_0 = \frac{\partial h}{\partial t} + \frac{\partial h}{\partial \check{X}}\frac{\partial \check{X}}{\partial t} = \frac{\partial h}{\partial t} + \frac{\partial h}{\partial \check{X}}U_0, \tag{3}$$

$$V_0 = \frac{\partial H}{\partial t} + \frac{\partial H}{\partial \check{X}}\frac{\partial \check{X}}{\partial t} = \frac{\partial H}{\partial t} + \frac{\partial H}{\partial \check{X}}U_0, \tag{4}$$

Eqs. (1) and (2) are used in (3) and (4) to obtain:

$$U_0 = \frac{-\frac{2\pi}{\lambda}ac\alpha\varepsilon\cos\left(\frac{2\pi}{\lambda}\right)(\check{X}-ct)}{1-\frac{2\pi}{\lambda}a\alpha\varepsilon\cos\left(\frac{2\pi}{\lambda}\right)(\check{X}-ct)}, \tag{5}$$

$$V_0 = \frac{\frac{2\pi}{\lambda}ac\varepsilon\sin\left(\frac{2\pi}{\lambda}\right)(\check{X}-ct)}{1-\frac{2\pi}{\lambda}a\alpha\varepsilon\cos\left(\frac{2\pi}{\lambda}\right)(\check{X}-ct)}. \tag{6}$$

Assumptions of the model

- The flow is incompressible.
- The fluid is modeled as an Ostwald–de Waele non-Newtonian fluid.
- The flow takes place within a porous medium-filled ciliated tube.
- Since the Reynolds number is low enough, inertial terms are neglected.
- The channel width is significantly smaller than the ciliary wave's wavelength.
- The electric potential is calculated using the Debye-

Hückel approximation.

- ◈ Thermal radiation is modeled using the Rosseland approximation.
- ◈ A magnetic field is applied to the flow. Electroosmotic effects are also included.
- ◈ Thermophoresis and Brownian motion are taken into consideration.
- ◈ The concentration equation takes activation energy into account.
- ◈ At the channel walls, suitable temperature, concentration, velocity and microorganism slip conditions are enforced.

The followings are the generic continuity, momentum, energy, concentration and gyrotactic microorganism equations for hybrid nanofluids [2-4]:

$$\nabla \cdot \boldsymbol{V} = 0, \tag{7}$$

$$\rho_{hnf}\frac{d\boldsymbol{V}}{dt}$$

$$= -\nabla \boldsymbol{P} + \nabla \cdot \boldsymbol{\tau} + (\boldsymbol{J} \times \boldsymbol{B}) - \frac{\mu_{hnf}}{K}\boldsymbol{V} + \rho_e \boldsymbol{E} + \boldsymbol{g}(\rho\beta)_{hnf}(T - T_0)(1 - C_0)$$

$$-\boldsymbol{g}(\rho_p - \rho_f)(C - C_0) - \boldsymbol{g}\gamma(\rho_m - \rho_f)(N - N_0), \tag{8}$$

$$(\rho c_p)_{hnf}\frac{dT}{dt} = k_{hnf}\nabla^2 T - \nabla \cdot q_r + (\rho c_p)_p\left(D_B(\nabla C \cdot \nabla T) + \frac{D_T}{T_m}(\nabla T)^2\right)$$

$$+\frac{\mu_{hnf}}{K}\boldsymbol{V}^2, \tag{9}$$

$$\frac{dC}{dt} = D_B\nabla^2 C + \frac{D_T}{T_m}\nabla^2 T - k_r^2(C - C_0)\left(\frac{T}{T_0}\right)^n exp\left(\frac{-E_a}{\omega T}\right), \tag{10}$$

$$\frac{dN}{dt} = D_m\nabla^2 N - \frac{b_* W_c}{\Delta C}\nabla \cdot (N\nabla C). \tag{11}$$

The Ostwald de Waele fluid model's stress tensor can be defined in the following manner [37]:

$$\boldsymbol{\tau} = \mu_{hnf} \mid \dot{\gamma} \mid^{m-1} A_1. \tag{12}$$

where m is the power law index and μ_{hnf} is the flow consistency index.

The strain rate tensor's second invariant $\dot{\gamma}$ is given as:

$$\dot{\gamma} = \sqrt{\frac{1}{2}tr(A_1^2)}. \tag{13}$$

The velocity components are $\breve{U}$ in $\breve{X}$ direction and $\breve{V}$ in $\breve{Y}$ direction, correspondingly.

The Poisson equation is outlined as [24-26]:

$$\nabla^2 \breve{\Phi} = -\frac{\rho_e}{\varepsilon_f}. \tag{14}$$

where the electrolyte's net charge density is ρ_e and the dielectric constant is represented by ε_f. It may seem as follows:

$$\rho_e = ze(\breve{n}_+ - \breve{n}_-). \tag{15}$$

The symbols z, e, $\breve{n}_+$ and $\breve{n}_-$, stand for charge balance, charge, positive and negative ions, sequentially. The Boltzmann distribution is as follows:

$$\breve{n}_+ = n_0 e^{\frac{-ze\breve{\Phi}}{\breve{k}_B\breve{T}_v}}, \quad \breve{n}_- = n_0 e^{\frac{ze\breve{\Phi}}{\breve{k}_B\breve{T}_v}}. \tag{16}$$

Put Eq. (16) in Eq. (15) to get

$$\rho_e = -2zen_0 \sinh\left(\frac{ze\breve{\Phi}}{\breve{k}_B\breve{T}_v}\right). \tag{17}$$

By Debye-Huckel linearization

$$\sinh\left(\frac{ze\breve{\Phi}}{\breve{k}_B\breve{T}_v}\right) \approx \left(\frac{ze\breve{\Phi}}{\breve{k}_B\breve{T}_v}\right). \tag{18}$$

Now Eq. (17) becomes

$$\rho_e = -2zen_0\left(\frac{ze\breve{\Phi}}{\breve{k}_B\breve{T}_v}\right). \tag{19}$$

The bulk concentration is connoted by n_0, valence by z, the Boltzmann constant by $\breve{k}_B$ and the absolute temperature by $\breve{T}_v$.

Comparing Eq. (14) and Eq. (19), we get

$$\nabla^2\breve{\Phi} = \frac{2(ze)^2 n_0}{\varepsilon_f \breve{k}_B\breve{T}_v}\breve{\Phi}. \tag{20}$$

Using the Rosseland diffusion technique, the radiative flux for radiation q_r, specified in Eq. (9) is found as follows:

$$q_r = -\frac{4\sigma_*}{3k_*}\nabla T^4. \tag{21}$$

Taylor expansion on T^4 with respect to T_0 is now defined as:

$$T^4 = T_0^4 + 4T_0^3(T - T_0) + 6(T - T_0)^2 + \ldots \tag{22}$$

By eliminating higher terms of T in $(T - T_0)$, we get

$$T^4 = 4T_0^3 T - 3T_0^4. \tag{23}$$

Then we get in Eq. (25),

$$\nabla \cdot q_r = -\frac{16\sigma_* T_0^3}{3k_*}\nabla^2 \mathrm{T}. \tag{24}$$

where k_* and σ_* implies Rosseland mean absorption, and Stephan-Boltzmann constant.

The following formulas for different forms are used to apply the hybrid nanofluid's thermophysical properties in the current investigation [11-13]:

$$\mu_{hnf} = \frac{\mu_f}{((1-\breve{\varphi}_1)(1-\breve{\varphi}_2))^{2.5}}, \tag{25}$$

$$\begin{aligned}
\sigma_{hnf} &= \sigma_{bf}\left(\frac{\sigma_2(1+2\breve{\varphi}_2)+2\sigma_{bf}(1-\breve{\varphi}_2)}{\sigma_2(1-\breve{\varphi}_2)+\sigma_{bf}(2+\breve{\varphi}_2)}\right),\\
\sigma_{bf} &= \sigma_f\left(\frac{\sigma_1(1+2\breve{\varphi}_1)+2\sigma_f(1-\breve{\varphi}_1)}{\sigma_1(1-\breve{\varphi}_1)+\sigma_f(2+\breve{\varphi}_1)}\right),
\end{aligned} \tag{26}$$

$$\rho_{hnf} = \rho_f\left((1-\breve{\varphi}_2)\left(1-\breve{\varphi}_1+\frac{\breve{\varphi}_1\rho_1}{\rho_f}\right)+\frac{\breve{\varphi}_2\rho_2}{\rho_f}\right), \tag{27}$$

$$(\rho\beta)_{hnf} = (\rho\beta)_f\left((1-\breve{\varphi}_2)\left(1-\breve{\varphi}_1+\frac{\breve{\varphi}_1(\rho\beta)_1}{(\rho\beta)_f}\right)+\frac{\breve{\varphi}_2(\rho\beta)_2}{(\rho\beta)_f}\right), \tag{28}$$

$$\begin{aligned}
k_{hnf} &= k_{bf}\left(\frac{k_2+(s-1)k_{bf}-(s-1)\breve{\varphi}_2(k_{bf}-k_2)}{k_2+(s-1)k_{bf}+\breve{\varphi}_2(k_{bf}-k_2)}\right),\\
k_{bf} &= k_f\left(\frac{k_1+(s-1)k_f-(s-1)\breve{\varphi}_1(k_f-k_1)}{k_1+(s-1)k_f+\breve{\varphi}_1(k_f-k_1)}\right),
\end{aligned} \tag{29}$$

where s stands for shape factor (s = 5.7 for platelets), $\breve{\varphi}_1$ and $\breve{\varphi}_2$ for nanoparticles' volume fractions and subscripts 1 and 2 for silver and gold, respectively. Additionally, Table 1 lists the base fluid's and nanoparticles' physical characteristics.

Eqs. (7)-(11) are simplified by transitioning the flow perusal from research frame to the wave-associated frame using the transformations listed below.

Table 1. Various nanoparticle and base fluid properties.

Fluid/Particle	σ (S/m)	k (W/m K)	ρ (kg/m^3)	$\beta\times 10^{-6}$ (K^{-1})
Blood	0.7	0.52	1060	300
Silver	3.6× 10^7	429	10500	189/10
Gold	4.1× 10^6	328	19300	14

$$\begin{aligned}
&\bar{X} = \breve{X} - ct,\ \bar{Y} = \breve{Y},\ \bar{U} = \breve{U} - c,\ \bar{V} = \breve{V},\ \bar{T} = \breve{T},\\
&\bar{C} = \breve{C},\ \bar{N} = \breve{N},\ \bar{p} = \breve{p}.
\end{aligned} \tag{30}$$

Defining dimensionless parameters in the expressions below:

$$\begin{aligned}
&x = \frac{\bar{X}}{\lambda}, y = \frac{\bar{Y}}{a}, v = \frac{\bar{V}}{\delta c}, u = \frac{\bar{U}}{c}, p = \frac{a^2\bar{p}}{\mu_f c\lambda}, \delta = \frac{a}{\lambda}, \varepsilon = \frac{b}{a},\\
&Re = \frac{c\rho_f a}{\mu_f}, \sigma = \frac{\bar{C}-C_0}{C_1-C_0}, \theta = \frac{\bar{T}-T_0}{T_1-T_0}, \gamma = \frac{\bar{N}-N_0}{N_1-N_0}, \Phi = \frac{\bar{\Phi}}{\zeta},\\
&\xi = \frac{k_r^2 a^2\rho_f}{\mu_f}, Pr = \frac{c_{pf}\mu_f}{k_f}, Hr = B_0 a\sqrt{\frac{\sigma_f}{\mu_f}}, Rn = \frac{16\sigma_* T_0^3}{3k_* c_{pf}\mu_f},\\
&Sc = \frac{\mu_f}{D_B\rho_f}, \tau = \frac{a\bar{\tau}}{c\mu_f}, Lb = \frac{\mu_f}{D_m\rho_f}, Gr = \frac{ga^2(\rho\beta)_f(1-C_0)(T_1-T_0)}{\mu_f c},\\
&Nr = \frac{(\rho_p-\rho_f)(C_1-C_0)}{(\rho\beta)_f(1-C_0)(T_1-T_0)}, Rb = \frac{\gamma(\rho_m-\rho_f)(N_1-N_0)}{(\rho\beta)_f(1-C_0)(T_1-T_0)},\\
&N_b = \frac{(\rho c_p)_p\rho_f(C_1-C_0)D_B}{\mu_f(\rho c_p)_f}, N_t = \frac{(\rho c_p)_p\rho_f(T_1-T_0)D_T}{T_m\mu_f(\rho c_p)_f},\\
&\beta = \frac{T_1-T_0}{T_0}, E = \frac{E_a}{T_0\omega}, Pe = \frac{W_c b_*}{D_m}, \Omega = \frac{N_0}{N_1-N_0}, me = aez\sqrt{\frac{2n_0}{\varepsilon_f T_v k_B}},\\
&Uhs = \frac{-E_x\varepsilon_f\zeta}{\mu_f c}, \dot{\gamma} = \frac{\bar{\gamma}a}{c}, Da = \frac{K}{a^2}, Ec = \frac{c^2}{(T_1-T_0)c_{pf}}
\end{aligned} \tag{31}$$

Using wave transformation in Eq. (20). Then we have,

$$\frac{\partial^2\bar{\Phi}}{\partial\bar{X}^2}+\frac{\partial^2\bar{\Phi}}{\partial\bar{Y}^2} = \left(\frac{2(ze)^2 n_0}{\varepsilon_f\bar{k}_B\bar{T}_v}\right)\bar{\Phi}. \tag{32}$$

Using dimensionless parameters in the equation above, we have

$$\frac{\partial^2\Phi}{\partial y^2} = me^2\Phi. \tag{33}$$

The symbol *me* refers to the electroosmotic parameter. The relevant boundary conditions are composed as

$$\begin{aligned}
&\Phi(y) = 1 \text{ at } y = h,\\
&\Phi(y) = 0 \text{ at } y = -h.
\end{aligned} \tag{34}$$

Solving Eq. (33) with respect to Eq. (34), to get solution

$$\Phi = \frac{\sinh me(y+h)}{\sinh(2hme)}. \tag{35}$$

Using Eq. (30-31) in governing Eqs. (7-11) and incorporating lubrication theory (described mathematically as $Re \ll 1,\ \delta \ll 1$), we get

$$\begin{aligned}
0 = &-\frac{\partial p}{\partial x}+a_1\frac{\partial}{\partial y}\left[\left(\frac{\partial u}{\partial y}\right)^m\right]-a_2 Hr^2(u+1)-\frac{a_1}{Da}(u+1)\\
&+me^2\Phi Uhs+a_3 Gr\theta-GrNr\sigma-GrRb\gamma,
\end{aligned} \tag{36}$$

$$0 = -\frac{\partial p}{\partial y}, \tag{37}$$

$$0 = (a_4 + RnPr)\frac{\partial^2\theta}{\partial y^2} + N_b Pr\frac{\partial\theta}{\partial y}\frac{\partial\sigma}{\partial y} + N_t Pr\left(\frac{\partial\theta}{\partial y}\right)^2 + \frac{a_1}{Da}PrEc(u+1)^2. \tag{38}$$

$$0 = \frac{\partial^2\sigma}{\partial y^2} + \frac{N_t}{N_b}\frac{\partial^2\theta}{\partial y^2} - \xi Sc\sigma(1+\beta\theta)^n \exp\left(-\frac{E}{1+\beta\theta}\right), \tag{39}$$

$$0 = \frac{\partial^2\gamma}{\partial y^2} - Pe(\Omega+\gamma)\frac{\partial^2\sigma}{\partial y^2} - Pe\frac{\partial\sigma}{\partial y}\frac{\partial\gamma}{\partial y}. \tag{40}$$

The shear stresses are given as:

$$\tau_{yx} = \tau_{xy} = \frac{\mu_{hnf}}{\mu_f}\left(\frac{\partial u}{\partial y}\right)^m. \tag{41}$$

where coefficients in above equations are defined as:

$$a_1 = \frac{\mu_{hnf}}{\mu_f},\ a_2 = \frac{\sigma_{hnf}}{\sigma_f},\ a_3 = \frac{(\rho\beta)_{hnf}}{(\rho\beta)_f},\ a_4 = \frac{k_{hnf}}{k_f}. \tag{42}$$

Taking the derivative of Eq. (36) with respect to y and employing $u = \frac{\partial\Psi}{\partial y}$, we get

$$0 = a_1\frac{\partial^2}{\partial y^2}\left[\left(\frac{\partial^2\Psi}{\partial y^2}\right)^m\right] - a_2Hr^2\frac{\partial^2\Psi}{\partial y^2} - \frac{a_1}{Da}\frac{\partial^2\Psi}{\partial y^2} + me^2\frac{\partial\Phi}{\partial y}Uhs + a_3Gr\frac{\partial\theta}{\partial y} - GrNr\frac{\partial\sigma}{\partial y} - GrRb\frac{\partial\gamma}{\partial y}, \tag{43}$$

Now using dimensionless parameters, the boundary conditions are given as [3, 22]

$$\begin{aligned}
&\Psi = \frac{F}{2},\ \frac{\partial\Psi}{\partial y} = u = -\lambda_1 a_1\left(\frac{\partial u}{\partial y}\right)^m - 1 - 2\pi\alpha\delta\varepsilon\cos 2\pi x \quad at \quad y = h,\\
&\Psi = -\frac{F}{2},\ \frac{\partial\Psi}{\partial y} = u = \lambda_1 a_1\left(\frac{\partial u}{\partial y}\right)^m - 1 - 2\pi\alpha\delta\varepsilon\cos 2\pi x \quad at \quad y = -h,\\
&\theta + \lambda_2\frac{\partial\theta}{\partial y} = 0 \quad at \quad y = h,\\
&\theta - \lambda_2\frac{\partial\theta}{\partial y} = 1 \quad at \quad y = -h,\\
&\sigma + \lambda_3\frac{\partial\sigma}{\partial y} = 0 \quad at \quad y = h,\\
&\sigma - \lambda_3\frac{\partial\sigma}{\partial y} = 1 \quad at \quad y = -h,\\
&\gamma + \lambda_4\frac{\partial\gamma}{\partial y} = 0 \quad at \quad y = h,\\
&\gamma - \lambda_4\frac{\partial\gamma}{\partial y} = 1 \quad at \quad y = -h.
\end{aligned} \tag{44}$$

where $h = 1 + \varepsilon\cos 2\pi x$. Here $F = \int_{-h}^{h}\frac{\partial\Psi}{\partial y}dy$ is the wave formations' mean flow rate with time. The $Q = F + 1$ is mean flow rate.

3. Analytical Solution

With their corresponding slip boundary conditions Eq. (44), the nonlinear equations (36)-(40) are intricate and challenging differential equations. Such highly complicated nonlinear partial differential equations can be efficiently solved by the semi-analytic method that is homotopy perturbation method.

Let us construct Homotopy of the governing equations (36-40) as below [21, 38]:

$$\begin{aligned}
H(u,q) &= L(u) - L(u_0) + q(L(u) - \frac{\partial p}{\partial x} + 2a_1\frac{\partial u}{\partial y}\frac{\partial^2 u}{\partial y^2}\\
&- a_2Hr^2(u+1) + me^2\left(\frac{\sinh me(y+h)}{\sinh(2hme)}\right)Uhs + a_3Gr\theta\\
&- GrNr\sigma - GrRb\gamma - \frac{a_1}{Da}(u+1)) = 0
\end{aligned} \tag{45}$$

$$\begin{aligned}
H(\theta,q) &= L(\theta) - L(\theta_0) + q(L(\theta) + \frac{N_bPr}{(a_4+RnPr)}\frac{\partial\theta}{\partial y}\frac{\partial\sigma}{\partial y}\\
&+ \frac{N_tPr}{(a_4+RnPr)}\left(\frac{\partial\theta}{\partial y}\right)^2 + \frac{a_1PrEc}{Da(a_4+RnPr)}(u+1)^2) = 0,
\end{aligned} \tag{46}$$

$$\begin{aligned}
&H(\sigma,q) = L(\sigma) - L(\sigma_0)\\
&+q\left(L(\sigma) + \frac{N_t}{N_b}\frac{\partial^2\theta}{\partial y^2} - \xi Sc\sigma(1+\beta\theta)^n\exp\left(-\frac{E}{1+\beta\theta}\right)\right) = 0,
\end{aligned} \tag{47}$$

$$\begin{aligned}
&H(\gamma,q) = L(\gamma) - L(\gamma_0)\\
&+q\left(L(\gamma) - Pe(\Omega+\gamma)\frac{\partial^2\sigma}{\partial y^2} - Pe\frac{\partial\sigma}{\partial y}\frac{\partial\gamma}{\partial y}\right) = 0.
\end{aligned} \tag{48}$$

where $L = \frac{\partial^2}{\partial y^2}$ is the linear operator and q is an embedding parameter such that $q \in [0,1]$

Using following perturbation in above Eqs. (45)-(48),

$$\begin{aligned}
u &= \tilde{u}_0 + q\tilde{u}_1,\\
\theta &= \tilde{\theta}_0 + q\tilde{\theta}_1,\\
\sigma &= \tilde{\sigma}_0 + q\tilde{\sigma}_1,\\
\gamma &= \tilde{\gamma}_0 + q\tilde{\gamma}_1.
\end{aligned} \tag{49}$$

With regard to their slip boundary conditions, we solve these equations for only first two dominant orders' systems. The initial guesses are taken as

$$u_0 = -1 - \frac{hy}{a_1\lambda_1} - 2\pi\alpha\delta\varepsilon Cos[2\pi x],\ \theta_0 = \frac{h - y + \lambda_2}{2(h + \lambda_2)},$$
$$\sigma_0 = \frac{1}{2} - \frac{y}{2(h + \lambda_3)},\ \gamma_0 = \frac{h - y + \lambda_4}{2(h + \lambda_4)}.$$

Using the built-in DSolve tool in Mathematica software for $q = 1$ in Eq. (49) to find the final solutions as:

$$\begin{aligned} u = {} & -1 - \frac{hy}{a_1\lambda_1} - 2\pi\alpha\delta\varepsilon\cos(2\pi x) + \frac{1}{12a_1\lambda_1 Da(h+\lambda_2)(h+\lambda_3)(h+\lambda_4)} \\ & (y^3 A_1 + A_2 C[1] + 3a_1 yDa\lambda_1(h+\lambda_2)(h+\lambda_3)(h+\lambda_4) \\ & ((2\frac{dp}{dx} + Gr(-a_3 + Nr + Rb)))y + 4C[2]) - 12 \\ & a_1(a_1 + a_2 DaHr^2)y^2\pi\alpha\delta\varepsilon\cos(2\pi x)\lambda_1(h+\lambda_2) \\ & (h+\lambda_3)(h+\lambda_4) - 12a_1\lambda_1 DaUhs(h+\lambda_2)(h+\lambda_3) \\ & (h+\lambda_4)\mathrm{csch}(2hme)\sinh(me(h+y)))), \end{aligned} \tag{50}$$

$$\begin{aligned} \theta = {} & \frac{h - y + \lambda_2}{2(h+\lambda_2)} + C[3] + yC[4] + \frac{1}{24a_1\lambda_1^2 Da(h+\lambda_2)^2(h+\lambda_3)} \\ & (Pry^2(-2Ec(h^2y^2 + 12(a_1\pi\alpha\delta\varepsilon\lambda_1)^2))(h+\lambda_2)^2(h+\lambda_3) \\ & - 3a_1\lambda_1^2 Da(h(N_b + N_t) + N_b\lambda_2 + N_t\lambda_3) - \\ & 8a_1 Ec\pi\alpha\theta\varepsilon\lambda_1(h+\lambda_2)^2(h+\lambda_3)(2hy\cos(2\pi x) \\ & + 3a_1\pi\alpha\theta\varepsilon\lambda_1\cos(2\pi x)))), \end{aligned} \tag{51}$$

$$\begin{aligned} \sigma = {} & \frac{h - y + \lambda_3}{2(h+\lambda_3)} + C[5] + yC[6] - \frac{1}{96(h+\lambda_2)^2(h+\lambda_3)} \\ & Sc(\frac{3}{5}Eny^5\beta^2 - 6y^2(2 + E(-2+\beta))(2+n\beta)(h+\lambda_2)(h+\lambda_3) \\ & + 2y^3(h+\lambda_2)(h(4 + 4n\beta + E(-4 + \beta(4 - 4n + 3n\beta))) \\ & + (2 + E(-2+\beta))(2+n\beta)\lambda_2 + 2\beta(E + n - En + En\beta)\lambda_3) \\ & - y^4\beta(2n(h+\lambda_2) + E(h(2 - 2n + 3n\beta) + 2(1 + n(-1+\beta))\lambda_2 \\ & + n\beta\lambda_3)))\xi, \end{aligned} \tag{52}$$

$$\begin{aligned} \gamma = {} & \frac{h - y + \lambda_4}{2(h+\lambda_4)} + \frac{Pe(y^2 - h(h+2\lambda_4))}{8(h+\lambda_3)(h+\lambda_4)} + \frac{1}{1920(h+\lambda_2)^2(h+\lambda_3)^2(h+\lambda_4)} \\ & (y^6(5EhnPeSc\beta^2\xi + 5EnPeSc\beta^2\lambda_3\xi) + y^5 A_3 + y^4 A_4 + y^3 A_5 + y^2 A_6) \\ & + C[7] + yC[8], \end{aligned} \tag{53}$$

where the constants are given in "Appendix". The expression of $\frac{dp}{dx}$ in form of F can be elevated as:

$$\begin{aligned} \frac{dp}{dx} = {} & \frac{1}{10Dah^3me}(3DaFme + 5a_3 GrDah^3me - 5GrDah^3meNr \\ & - 5GrDah^3meRb - 3GrDahmeUhs + 12Dahme\pi\alpha\delta\varepsilon\cos(2\pi x) \\ & + 20a_1h^3me\pi\alpha\delta\varepsilon\cos(2\pi x) + 20a_2Dah^3Hr^2me\pi\alpha\delta\varepsilon\cos(2\pi x) \\ & + 3DaUhs\tanh(hme) + 6Dah^2m^2e^2Uhs\tanh(hme)). \end{aligned} \tag{54}$$

4. Results and Discussion

This section shows how different parameters have a physical impact on temperature, velocity, nanoparticle concentration and motile organism profiles. Additionally, pressure gradients, pressure rises and streamlines are displayed. Table 2 summarizes the ranges of the dimensionless parameters taken into consideration in the graphical analysis. These values are in accordance with closely related studies [26, 37] and are chosen to investigate the physical impacts of the relevant factors over an acceptable range.

4.1. Validation

In order to give validation of the current results, a detailed calculation is done as seen in Table 3. In the table, a limiting case of the current model ($m \to 1$,

Table 2. Ranges of the dimensionless parameters considered in the graphical analysis [37].

Parameters	Ranges	Parameters	Ranges
Uhs	1-3.2	*Gr*	0.1-2
ξ	1-1.6	*Rn*	0.5-2
Da	0.035-4	*Pe*	0.9-2
λ_1	0.2-3	*Sc*	0.1-1.8
λ_2	0.1-3.2	*Hr*	1-2
λ_3	0.2-3	*Nr*	1-3
λ_4	0.2-3.4	*Ec*	0.1-1.3
N_t	1-1.4	β	0.2-1.3
N_b	1-2	Ω	0.5-1.8
Pr	1.3-6.2	*Rb*	0.5-3.2
me	0.5-3	*E*	0-1

Table 3. Comparison of current velocity data with Alfwzan *et al.* [26].

y	Data of [26]	Current data of u when $m \to 1$, $Da \to \infty$, $(\lambda_1, \lambda_2, \lambda_3, \lambda_4) \to 0$	u when $m = 2$, $Da = 0.6$, $\lambda_1 = 3, \lambda_2, \lambda_3, \lambda_4 = 2$
-1.5	-1.00125	-1.00126	-6.38079
-1.2	-0.633228	-0.633229	-2.82887
-0.9	-0.277814	-0.277815	-0.355699
-0.6	0.0430006	0.0430007	1.25843
-0.3	0.306282	0.306283	2.1089
0.0	0.487444	0.487445	2.2229
0.3	0.559218	0.559219	1.59018
0.6	0.490098	0.490099	0.18009
0.9	0.241954	0.241955	-2.04952
1.2	-0.233664	-0.233665	-5.14638
1.5	-1.00125	-1.00126	-9.1616

$Da \to \infty$, $\lambda_1, \lambda_2, \lambda_3, \lambda_4 \to 0$). In this instance, ($\lambda_1, \lambda_2, \lambda_3, \lambda_4 \to 0$) correspond to no-slip circumstances, $Da \to \infty$ eliminates the porous-medium resistance and $m \to 1$ reduces the Ostwald–de Waele fluid to the Newtonian case. The current model is reduced to the corresponding configuration of the existing study under these restricting conditions [26]. As Table 3 illustrates, the velocity values acquired with HPM closely match the data published in [26]. It can be verified from the table that current values are in close agreement with the values obtained in [26] by using numerical method through NDSolve tool of Mathematica. This fact not only ensured the validity of the current model but also it established the great accuracy of the method HPM in comparison with NDSolve used in [26].

4.2. Variation of Velocity

Fig. 2(a)–(d) interprets the outcomes of the Helmholtz-Smoluchowski velocity *Uhs*, temperature slip parameter λ_2, Darcy number *Da* and Grash of number *Gr* on velocity distributions. As can be seen in Fig. 2(a), the velocity profile first increases as the *Uhs* inclines due to electroosmotic forces and then the flow's middle shows the reverse tendency. Fig. 2(b)–(d) calculates the opposite outcome of λ_2, *Da* and *Gr* compared to Fig. 2(a). The velocity of the hybrid nanofluid is higher at the right wall region ($y > 0$) due to the dominating electrokinetic and buoyancy forces. Conversely, the left wall region ($y < 0$) experiences reduced velocity because of the resisting effects of the ciliated channel. Higher λ_2 reduces wall friction by allowing the fluid to accelerate near the walls. Increased *Da* enhances flow by decreasing porous resistance. Larger *Gr* strengthens buoyancy forces by boosting the velocity near heated regions.

4.3. Variation of temperature

The Darcy number *Da* descends the temperature profile in Fig. 3(a) because the porous medium has less permeability, which modifies the heat transfer characteristics of the flow. However, as Fig. 3(b) portrays, an increase in the temperature slip factor λ_2 increases the temperature profile by reducing the heat transfer between the fluid and channel walls. The temperature rises as the Prandtl number (Pr) increases, as seen in Fig. 3(c). Lower thermal diffusivity in relation to momentum diffusivity is associated with a bigger (Pr), which decreases thermal diffusion and encourages heat retention in the fluid. Fig. 3(d) shows that increasing the Eckert number *Ec* enhances the

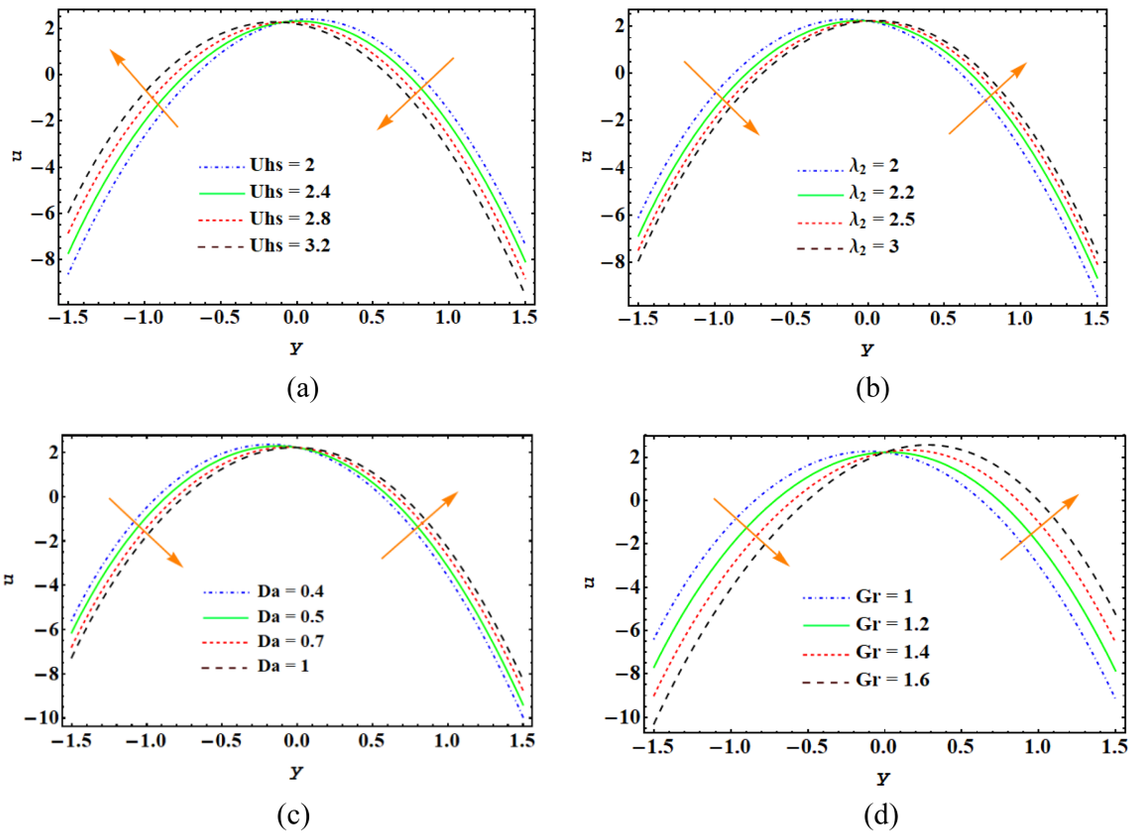


Fig. 2. (Color online) (a-d)Velocity distribution in 2D. The other parameters are fixed as: $Hr = 1$, $Rb = 1$, $x = 0.5$, $\lambda_1 = 3$, $n = 0.5$, $F = 0.02$, $Nr = 3$.

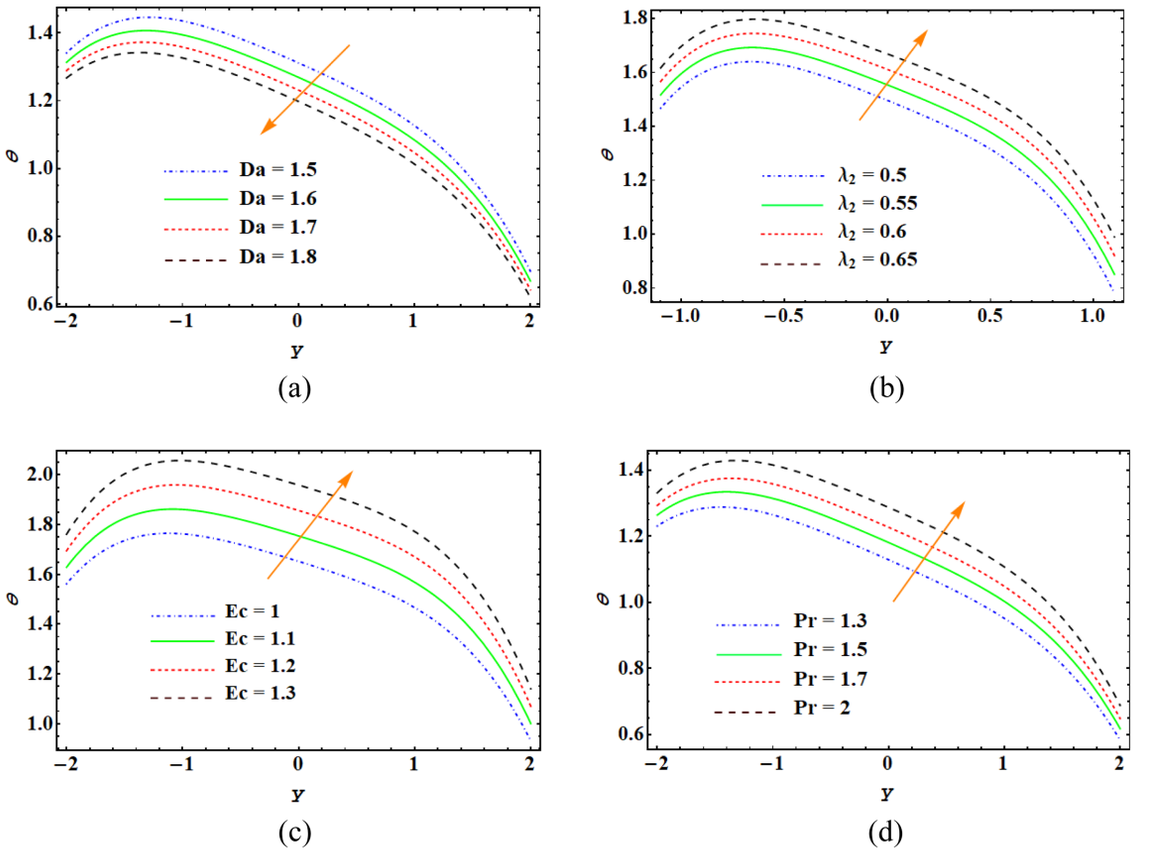


Fig. 3. (Color online) Temperature distributions for Da, λ_2, Ec and Pr within two coordinate schemes. The other parameters are fixed as: $\alpha = 0.2$, $\delta = 0.01$, $Nt = 1$, $Nb = 2$, $Rn = 2$, $x = 1$.

temperature profile. Since Ec represents the relative importance of kinetic-energy effects, its increase strengthens viscous dissipation and consequently increases the thermal energy of the fluid.

4.4. Variation of Nanoparticle Concentration

Significant physical implications are clarified by the analysis of the nanoparticle concentration profile. Fig. 4 shows the effects of temperature ratio, reaction rate, activation energy and the slip factor of nanoparticle concentration on concentration profile in the hybrid nanofluid. The slip factor of nanoparticle concentration λ_3 decreases the nanoparticle concentration profile by enhancing particle dispersion. This occurs because nanoparticles move more freely relative to the base fluid by reducing accumulation near the walls (see Fig. 4(a)). The concentration profile of nanoparticles diminishes as the temperature ratio β increases, as seen in Fig. 4(b). This fluctuation is linked to modifications in thermophoretic transport, which encourages the migration of nanoparticles from hotter areas to colder ones by changing the distribution of nanoparticles inside the channel. In Fig. 4(c), the concentration of nanoparticles drops as the reaction rate ξ increases. A lower concentration profile is the outcome of increased reaction-induced depletion, which is strengthened by a higher reaction rate in the concentration equation. Increasing the activation energy E raises the nanoparticle concentration profile, as shown in Fig. 4(d). Increased activation energy slows down the temperature-dependent chemical reaction, which lessens reaction-induced depletion and raises the concentration of nanoparticles.

4.5. Variation of motile microorganisms

Fig. 5 represents the effects of the slip factor of motile microorganisms, gape of concentration, Peclet number and Schmidt number on the profile of the hybrid nanofluid's motile microorganisms. From Fig. 5(a), a surge in the slip factor of gyrotactic motile microorganisms λ_4 reduces the motile microorganism profile. Enhanced slip promotes dispersion, prevents microorganisms from accumulating in specific regions and allows them to respond more freely to the surrounding hybrid nanofluid flow. Similarly in Fig. 5(b), motile organism profile

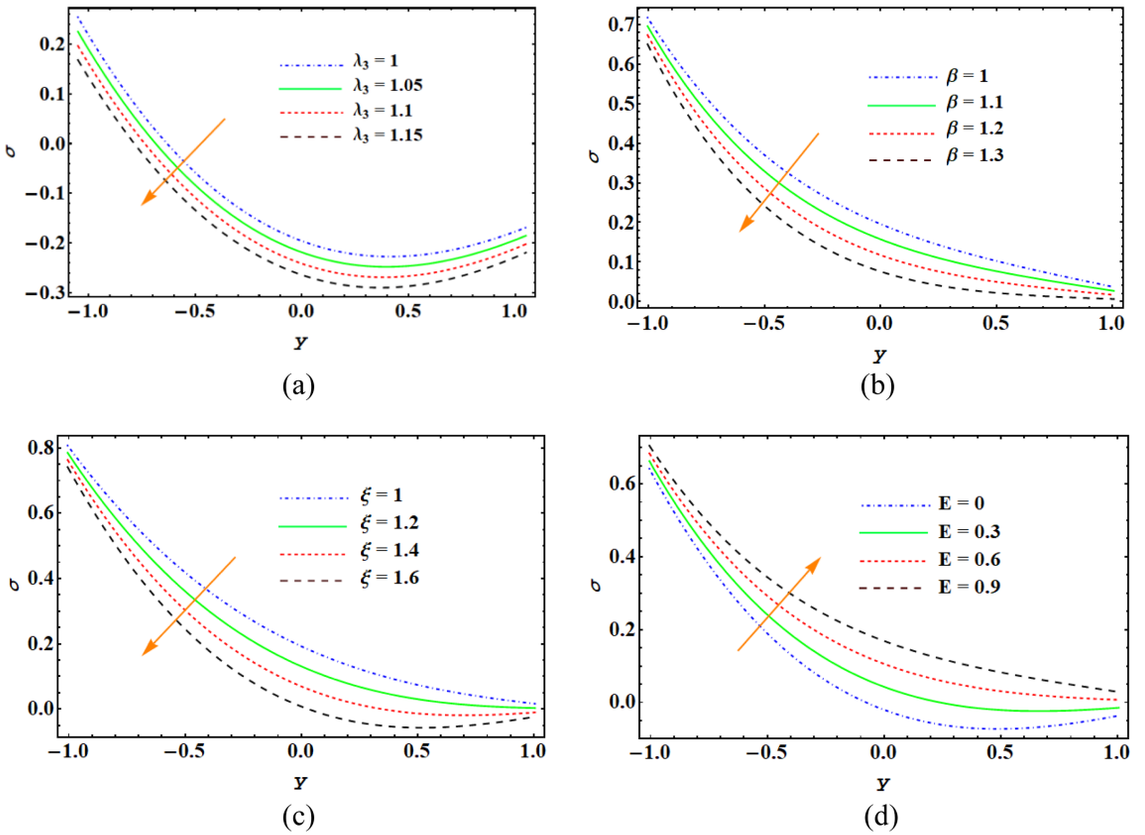


Fig. 4. (Color online) (a-d) Nanoparticle Concentration in 2D. The other parameters are fixed as: $n = 0.5$, $\lambda_2 = 0.2$, $x = 1$.

decreases as Ω rises. Physically, a larger gape of concentration Ω intensifies the concentration gradient by promoting microorganism movement from high concentration areas to low. Fall in motile microorganism profile is evident from Fig. 5(c) as the Peclet number *Pe* increases. This occurs because stronger convection carries microorganisms with the fluid by reducing their localized concentration and limiting accumulation in high-density regions. Additionally, a higher Schmidt number *Sc* limits mass diffusion by restricting microorganism movement and decreasing their profile as observed in Fig. 5(d).

4.6. Variation of Pressure Gradient

Fig. 6(a)–(d) showcases axial pressure gradient (*dp*/*dx*) distributions for Darcy number *Da*, Hartmann number *Hr*, Grashof number *Gr* and Helmholtz Smoluchowski velocity *Uhs*. In Fig. 6(a), it is clear that the Darcy number *Da* increases the pressure gradient in the channel center ($x \in [0.3, 0.7]$) due to enhanced permeability, which allows more fluid to pass through the porous medium. Near the walls ($x \in [0, 0.3]$) and ($x \in [0.7, 1]$), the pressure gradient decreases because flow resistance is reduced and less driving pressure is needed. In Fig. 6(b), opposite effects are shown. By increasing Hartman number *Hr*, as flow gets closer to the channel walls ($x \in [0, 0.3]$) and ($x \in [0.7, 1]$), the pressure gradient accelerates due to magnetic damping, while lowering it in the channel's central part ($x \in [0.3, 0.7]$) where the Lorentz force slows the flow. As can be seen in Fig. 6(c), the Grashof number Gr decreases the pressure gradient because buoyancy-driven convection promotes fluid motion and lessens the need for pressure-driven flow. Conversely, Fig. 6(d) shows that the pressure gradient increases by elevating Helmholtz–Smoluchowski velocity *Uhs*. The stronger electroosmotic forcing modifies the balance between electroosmotic and pressure-driven transport which results in an increased axial pressure-gradient distribution.

4.7. Variation of Pressure Rise

The pressure-rise profiles are shown in Fig. 7. Fig. 7(a) demonstrates that the pressure rise increases with the Grashof number *Gr*. This behavior is attributed to the enhanced buoyancy force associated with increasing *Gr*, which contributes to the fluid motion and consequently modifies the pressure-gradient distribution along the channel. In contrast, Fig. 7(b) shows that the pressure rise decreases as the electroosmotic parameter *me* increases.

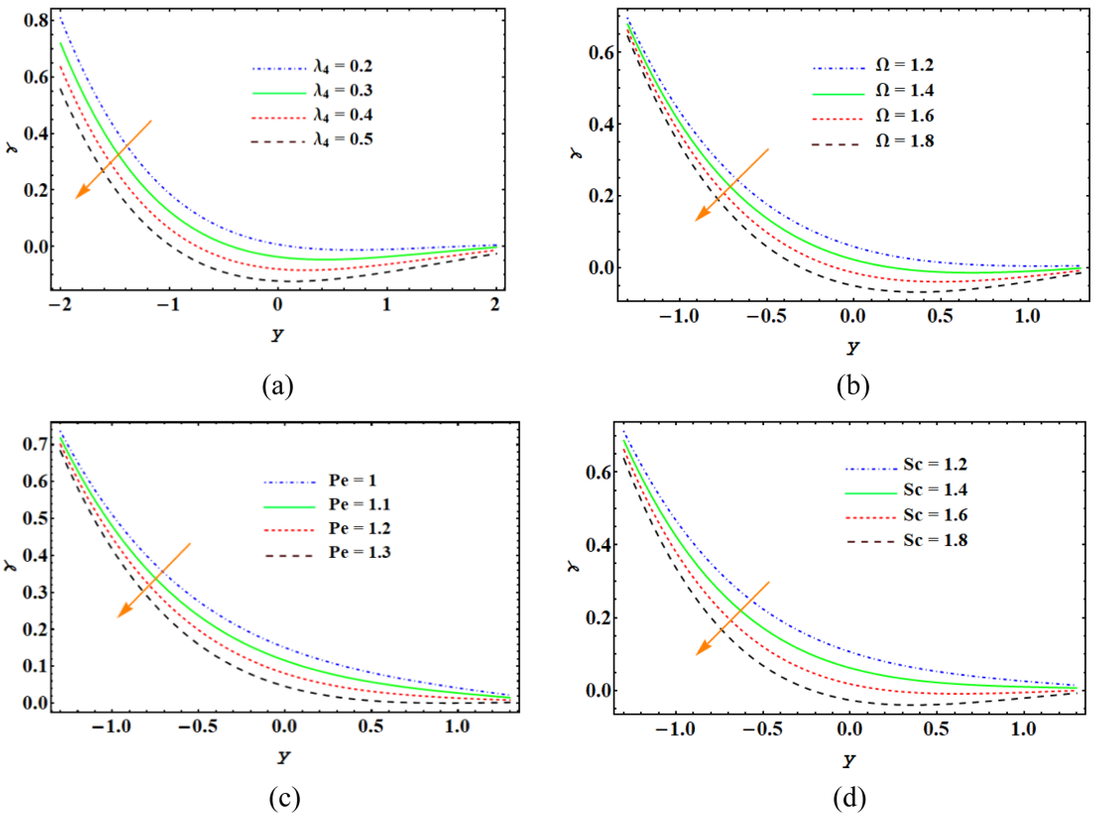


Fig. 5. (Color online) Microorganisms' distribution in 2D coordinates. The other parameters are fixed as: $\lambda_2 = 0.2$, $E = 1$, $\beta = 0.5$, $\xi = 1$, $\lambda_3 = 0.2$, $x = 1$.

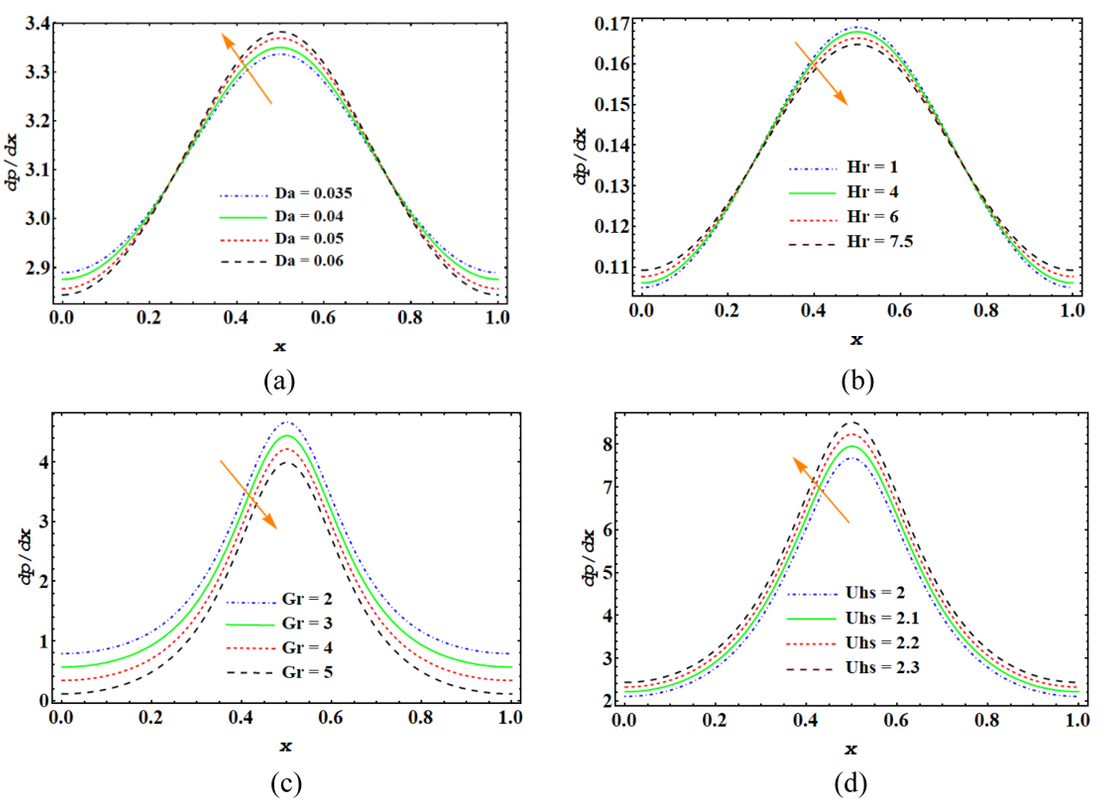


Fig. 6. (Color online) Pressure Gradient Graphs by varying (a) *Da*, (b) *Hr*, (c) *Gr*, (d) Uhs. The other parameters are fixed as: *Rb* = 0.5, *F* = 1, *Nr* = 1.

The stronger electroosmotic forcing enhances fluid transport by reducing the pressure gradient required to maintain the flow. Fig. 7(c) illustrates the influence of the cilia length parameter ε on the pressure rise in the two pumping zones. In the enhanced pumping region ($Q > 0$, $\Delta P < 0$), an increase in cilia length strengthens cilia-induced fluid transport and consequently reduces the required pressure rise. In the retrograde pumping region ($Q < 0$, $\Delta P > 0$), longer cilia increase the resistance associated with the backward flow by resulting in an increase in the pressure rise. These results demonstrate the role of ciliary motion in regulating pressure-driven transport in biological and microfluidic systems.

4.8. Variation of Streamlines

Trapping is a crucial aspect of cilia-induced transport, where a collection of closed streamlines creates a trapped bolus with a limited fluid volume. The trapping behavior is illustrated in Fig. 8(a)-(i) for different values of the velocity slip parameter λ_1, Rayleigh constant Rb and Darcy number Da. In Fig. 8(a)–(c), the streamlines' behavior for the velocity slip parameter is shown. Increasing λ_1 improves fluid mobility by lowering the resistance related to fluid motion at the channel walls. As a result, a bigger fluid bolus becomes trapped inside the channel and the closed-streamline region grows. Fig. 8(d)–(f) demonstrate that increasing the Rayleigh parameter Rb reduces the size of the trapped bolus. The impact of the Darcy number Da is depicted in Fig. 8(g)–(i). Reduced barrier to fluid motion and increased porous-medium permeability are correlated with an increase in Da. The trapped bolus contracts as a result of the ensuing increase in fluid mobility weakening the closed-streamline structure. The trapped bolus may vanish and the closed streamlines gradually weaken at big enough Da by suggesting suppression of the trapping phenomena. Overall, the streamline patterns show that the creation and size of trapped boluses are influenced by ciliary motility, buoyancy effects and porous-medium permeability. In cilia-driven microfluidic systems, these mechanisms are crucial for regulating fluid flow and trapping.

5. Conclusion

The research establishes a comprehensive theoretical framework which explains electromagnetohydrodynamic bioconvective transport for magnetized Ostwald–de Waele hybrid nanofluids flowing through a ciliated porous

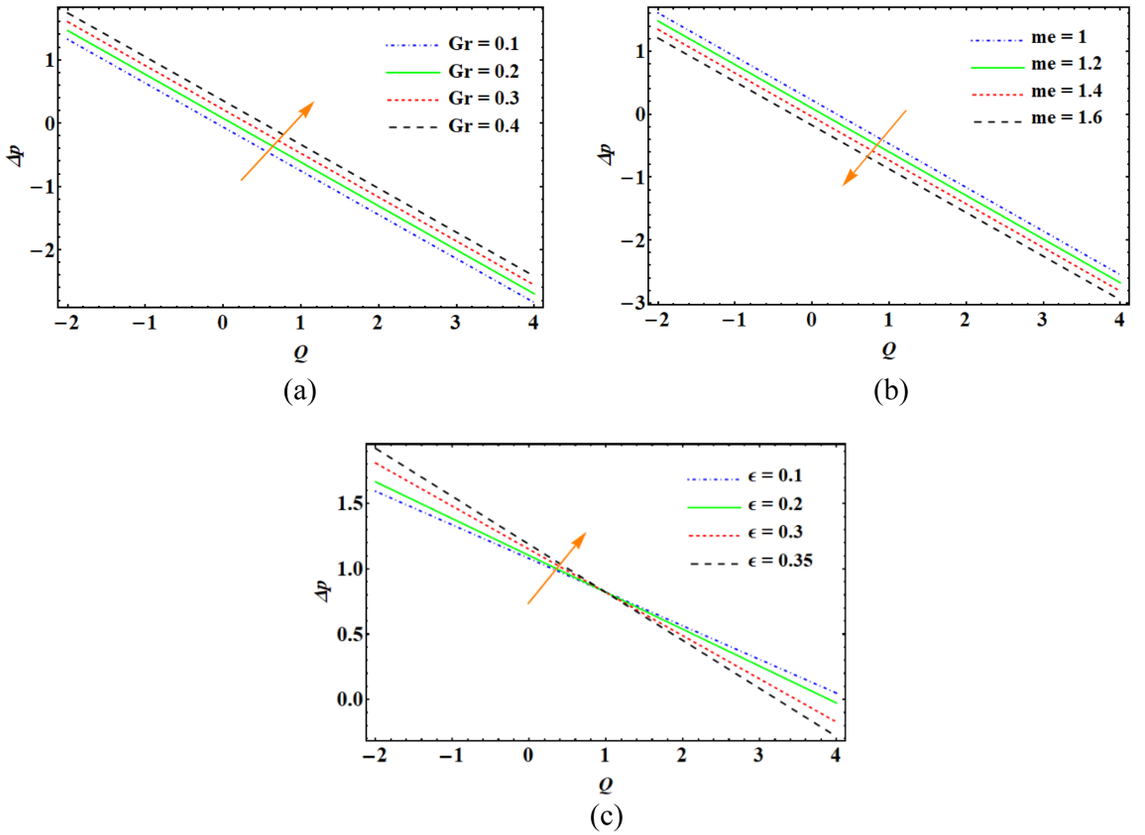


Fig. 7. (Color online) Pressure Rise by varying (a) *Gr*, (b) *me*, (c) *ε*. The other parameters are fixed as: $Da = 0.2$, $Rb = 2$, $Hr = 1$, $Uhs = 1$, $Nr = 2$.

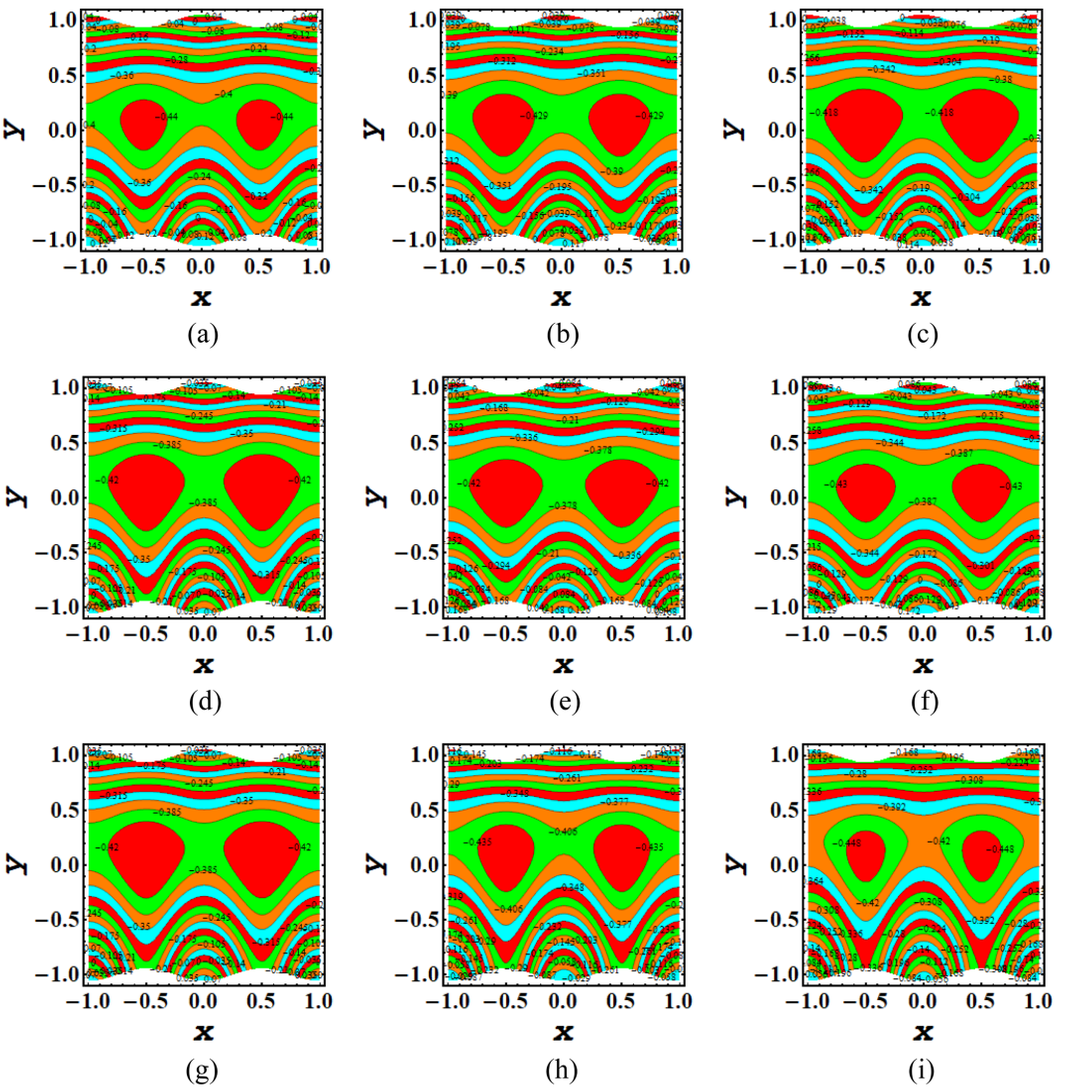


Fig. 8. (Color online) (a-c) 2D Streamlines for $\lambda_1 = 2$, 2.2, and 2.4 with $\lambda_2 = 1$, $\lambda_3 = 2$, and $\lambda_4 = 3$ fixed. (d-f) 2D Streamlines for *Da* = 2, 3, and 3.2, with *Da* = 2, *me* = 1, and *Gr* = 2 fixed. (g-i) 2D Streamlines for *Da* = 2, 3, and 4, with *Hr* = 1, *Rb* = 2, and *Nr* = 1 fixed.

microchannel. The model demonstrates the main physical mechanisms which drive biologically inspired microfluidic transport through its combination of electroosmosis with activation energy and thermal radiation and gyrotactic microorganism dynamics. From detailed discussion and graphical description, we have summed up the following major findings:

- The research findings show that ciliary motion together with electroosmotic forces determine flow asymmetry and pumping efficiency but power-law rheology as a non-Newtonian fluid affects shear-driven transport.
- The addition of activation energy functions as a stabilizing element which maintains nanoparticle levels by preventing reaction-driven depletion and boosting nanoparticle stability within reactive environments.
- The bioconvective system achieves stability through the combination of microorganism slip parameters with convective transport parameters which control the movement of motile cells.
- The system maintains control over its pressure characteristics and trapping behavior through the combined influence of magnetic damping and porous resistance.
- The proposed framework offers users a deep understanding of physical principles while providing an adaptable system which allows designers to create sophisticated bio-inspired microfluidic and biomedical transport systems.

Limitations and Future Work: Even though the current study produced valuable results, there are few limitations

that should be noted. There is no experimental confirmation in the analysis, which is based on a theoretical mathematical model. Furthermore, the model's application to certain flow regimes is limited by the long-wavelength and low Reynolds number assumptions. Simplified depictions of thermal-radiation and electrokinetic effects can also be obtained by using the Rosseland and Debye-Hückel approximation. Moreover, the current analysis may not accurately reflect all physiological and microfluidic situations because it takes into account certain fluid, nanoparticle and channel features. Future research could build upon the current model by adding more physiological impacts, more intricate channel geometries, broader nanoparticle properties and experimental validation.

Funding Declaration: This research work was supported by the Ministry of Education – Kingdom of Saudi Arabia through the project number 0038-1446-S.

Clinical trial number: Not applicable

Ethical Approval: No ethical approval was required for this study.

Consent to Participate: Not applicable

Consent to Publish: Not applicable.

Acknowledgement

The authors extend their appreciation to the Deputyship for Research & Innovation, Ministry of Education in Saudi Arabia for funding this research work through the project number 0038-1446-S.

Data availability statement: All data generated or analyzed during this study are included in this article.

Author Contribution declaration

Y. K., S. A., A. R., developed the mathematical modeling, suggested the solution of the problem, written the manuscript and supervised the project. A. M., S. U. K., A. A., developed analysis of mathematical simulation of the proposed problem, Solved the problem, revised the manuscript, S. A., A. R., A. M., examined the theory validation, drawn the graphical conclusion.

The manuscript was written through the contribution of all authors. All authors discussed the results, reviewed, and approved the final version of the manuscript.

Nomenclature

Dimensional Symbols Definition with SI units

a : Mean half width (m)
ε_f : Dielectric constant ($CV^{-1}m^{-1}$)
ω : Boltzmann constant ($Jmol^{-1}K^{-1}$)
g : Acceleration induce by the gravity (ms^{-2})
ε : Dimensionless quantity w.r.t a
c : Wave velocity (ms^{-1})
W_c : Swimming speed of the cell (ms^{-1})
T_m : Mean temperature (K)
E_a : Activation energy ($Jmol^{-1}$)
D : Diffusion coefficient (m^2s^{-1})
b_* : Chemotaxis constant (m)
k_r : Reaction rate (s^{-1})
λ : Wavelength (m)
E_X : Electrical field (Vm^{-1})
ρ : Density (kgm^{-3})
ρ_e : Net charge density (cm^{-3})
$\rho\beta$: Thermal expansion (kgm^{-3} K^{-1})
ρc_p : Effective heat capacity (Jm^{-3} K^{-1})
k : Thermal conductivity (Wm^{-1} K^{-1})
ζ : Zeta potential (V)
K : Porosity parameter (m^2)
$\check{U}, \check{V}$: Velocity in X, Y direction (ms^{-1})
$\check{C}$: Nanoparticle volume fraction
$\check{N}$: Motile organism
$\check{T}$: Temperature (K)
D_B : Brownian motion diffusion (m^2 s^{-1})
D_T : Thermophoretic diffusion (m^2 s^{-1} K^{-1})

Dimensionless symbols Definition

γ : Dimensionless motile organism
θ : Temperature
σ : Volume fraction of nanoparticle
Ω : Concentration gap for microorganisms
β : Ratio of temperatures
m : Power law index
n : Fitted rate
N_t : Thermophoresis parameter
N_b : Brownian motion parameter
Pr : Prandtl number
Ec : Eckert number
Rb : Rayleigh constant
Da : Darcy number
Lb : Bioconvection Lewis number
Sc : Schmidt number
Re : Reynold number
ξ : Dimensionless reaction rate
Hr : Hartmann number
Nr : Buoyancy number
Rn : Radiation parameter
Gr : Grashof number
Pe : Peclet number
Uhs : Helmholtz–Smoluchowski velocity
me : Electroosmotic parameter
$\lambda_1, \lambda_2, \lambda_3, \lambda_4$: Slip parameters

Subscripts	**Definition**
m	: Microorganism
f	: Nanofluid
p	: Nanoparticle
hnf	: Hybrid nanofluid

References

[1] M. S. Arslan, Z. Abbas, and M. Y. Rafiq, Adv. Mech. Eng. **15**, 16878132231157179 (2023).
[2] A. M. Siddiqui, A. A. Farooq, and M. A. Rana, Magnetohydrodynamics **50**, 109 (2014).
[3] S. Munawar and N. Saleem, Coatings **10**, 414 (2020).
[4] Z. Asghar, K. Javid, M. Waqas, A. Ghaffari, and W. A. Khan, Fluid Dyn. Res. **52**, 015514 (2020).
[5] M. M. Channakote, C. Siddabasappa, and D. Tripathi, Int. J. Comput. Mater. Sci. Eng. **14**, 2450006 (2025).
[6] S. Sam, M. M. Channakote, O. A. Bég, and T. A. Bég, Case Stud. Therm. Eng. **74**, 106995 (2025).
[7] S. A. Hussein, S. E. Ahmed, and A. A. M. Arafa, Eng. Sci. Technol. Int. J. **62**, 101956 (2025).
[8] S. U.-S. Choi and J. A. Eastman, Enhancing Thermal Conductivity of Fluids with Nanoparticles. ASME International Mechanical Engineering Congress & Exposition, San Francisco, 99 (1995).
[9] M. Sheikholeslami, J. Mol. Liq. **263**, 472 (2018).
[10] F. Hussain, M. Nazeer, M. Altanji, A. Saleem, and M. M. Ghafar, Case Stud. Therm. Eng. **28**, 101433 (2021).
[11] A. Almaneea, Alex. Eng. J. **61**, 8343 (2022).
[12] S. A. A. Shah, A. U. Awan, B. Ali, and A. E. Ragab, Numer. Heat Transf. A Appl. **86**, 6462 (2025).
[13] G. Huminic and A. Huminic, Int. J. Heat Mass Transf. **125**, 82 (2018).
[14] M. H. Ahmadi, M. Ghazvini, M. Sadeghzadeh, M. A. Nazari, and M. Ghalandari, Nano-Struct. Nano-Objects **20**, 100386 (2019).
[15] R. Adhikari, S. Das, and S. Das, Eng. Appl. Artif. Intell. **136**, 109048 (2024).
[16] X. Cheng, H. Sun, X. Xu, A. Wan, K. Al-Bukhaiti, J. Jiang, and Xiaosheng Ji, J. Magn. Magn. Mater. **655**, 174316 (2026).
[17] L. Ye, H. She, C. Sun, X. Wang, C. Liu, and C. Shi, Int. Commun. Heat Mass Transf. **172**, 110305 (2026).
[18] W. N. Mutuku and O. D. Makinde, Comput. Fluids **95**, 88 (2014).
[19] S. Ahmad, M. Ashraf, and K. Ali, Heliyon **6**, e05832 (2020).
[20] S. E. Ahmed, A. A. M. Arafa, and S. A. Hussein, Int. J. Model. Simul. **45**, 68 (2025).
[21] M. Ajithkumar, R. Meenakumari, G. Sucharitha, M. Vinodkumar Reddy, K. Javid, and P. Lakshminarayana, J. Appl. Phys. **135**, 194701 (2024).
[22] T. Hayat, A. Aziz, T. Muhammad, and A. Alsaedi, J. Therm. Anal. Calorim. **136**, 1769 (2019).
[23] V. Jagadesh, S. Sreenadh, M. Ajithkumar, G. Sucharitha, and P. Lakshminarayana, Radiat. Eff. Defects Solids **179**, 1162 (2024).
[24] B. Souayeh, K. Ramesh, N. Hdhiri, E. Yasin, M. W. Alam, K. Alfares, and A. Yasin, Nanomaterials **12**, 1615 (2022).
[25] J. Prakash, D. Tripathi, O.A. Bég, V. Srivastava, J. Porous Media **25**, 1 (2022).
[26] W. F. Alfwzan, A. Imran, F. M. Allehiany, and M. S. Aldhabani, Case Stud. Therm. Eng. **49**, 103252 (2023).
[27] S. Dolui, B. Bhaumik, and S. De, Math. Comput. Simul. **232**, 17 (2025).
[28] Y. Xu, K. Ju, and C. Zhang, Cyborg Bionic Syst. **5**, 0111 (2024).
[29] Y. Zhou, Z. Cai, Q. Li, C. Cui, P. Cao, S. Shao, and M. Sun, Aerosp. Sci. Technol. **177**, 112260 (2026).
[30] M. Ajithkumar and P. Lakshminarayana, ZAMM **104**, e202300007 (2024).
[31] D. S. Loenko, A. Shenoy, and M. A. Sheremet, Energies **12**, 2149 (2019).
[32] M. Ajithkumar, P. Lakshminarayana, and K. Vajravelu, J. Appl. Phys. **134**, 154701 (2023).
[33] M. M. Channakote, S. Marudappa, O. A. Bég, M. Narayana, and C. Siddabasappa, Results Eng. **26**, 104739 (2025).
[34] S. A. Hussein, Int. J. Model. Simul. **45**, 801 (2025).
[35] S. A. Hussein, A. A. M. Arafa, A. Elshekhipy, and N. H. Almalki, Numerical Heat Transfer, Part A: Applications **86**, 2569 (2025).
[36] B. Mal, S. Dolui, B. Bhaumik, and S. De, Electromagn. Biol. Med. **44**, 79 (2025).
[37] W. Jamshed, M. R. Eid, S. M. Hussain, A. Abderrahmane, R. Safdar, O. Younis, and A. A. Pasha, Int. Commun. Heat Mass Transf. **134**, 106038 (2022).
[38] K. Thirunavukarasan and G. Sucharitha, Case Stud. Therm. Eng. **66**, 105708 (2025).
[39] T. Hussain, O. A. Bég, S. Kuharat, T. A. Bég, and M. M. Bhatti, J. Comput. Appl. Mech. **57**, 443 (2026).
[40] A. Yusuf, M. M. Bhatti, R. Ellahi, and H. F. Öztop, Int. J. Numer. Methods Heat Fluid Flow, 1 (2026).

Appendix

$$C[1]=-\frac{1}{4}(-3Dah^2\left(2\frac{dp}{dx}+Gr(-a_3+Nr+Rb)\right)-2DaUhs$$
$$+12h^2(a_1+a_2DaHr^2)\pi\alpha\delta\varepsilon\cos(2\pi x)+4DahmeUhs\tanh(hme)),$$

$$C[2]=\frac{1}{12a_1\lambda_1Dah(h+\lambda_2)(h+\lambda_3)(h+\lambda_4)}(-5A_1h^3-6a_1DaUhs\lambda_1(h+\lambda_2)$$
$$(h+\lambda_3)(h+\lambda_4)+12a_1meUhsDah(h+\lambda_2)(h+\lambda_3)(h+\lambda_4)\coth(hme)),$$

$$C[3]=\frac{-1}{24a_1Da\lambda_1^{\,2}(a_4+RnPr)(h+\lambda_2)^2(h+\lambda_3)}(-hPr(2Ec(h+\lambda_2)^2(h^5+12a_1^{\,2}h\pi^2(\alpha\delta\varepsilon\lambda_1)^2$$
$$+4h^4\lambda_2+24a_1^{\,2}\pi^2(\alpha\delta\varepsilon\lambda_1)^2\lambda_2)(h+\lambda_3)-3a_1Da\lambda_1^{\,2}(h+2\lambda_2)(h(N_b+N_t)+N_b\lambda_2+N_t\lambda_3)$$
$$+24a_1^{\,2}Ec\pi^2(\alpha\delta\varepsilon\lambda_1)^2(h+\lambda_2)^2(h+2\lambda_2)(h+\lambda_3)\cos(4\pi x))),$$

$$C[4]=\frac{-2Ech^3Pr\pi\alpha\delta\varepsilon(h+3\lambda_2)\cos(2\pi x)}{3Da\lambda_1(a_4+RnPr)(h+\lambda_2)},$$

$$C[5]=\frac{-1}{96(h+\lambda_2)^2(h+\lambda_3)}hSc(h^4(24+14n\beta+E(-24+\beta(14-14n+9n\beta))))$$
$$+12(2+E(-2+\beta))(2+n\beta)\lambda_2^{\,2}\lambda_3^{\,2}+6h(2+E(-2+\beta))(2+n\beta)\lambda_2\lambda_3(3\lambda_2+4\lambda_3)$$
$$+h^3(2(24+13n\beta+E(-24+\beta(13-13n+7n\beta)))\lambda_2+(72+44n\beta+E(-72+\beta(44-44n+31n\beta)))\lambda_3)$$
$$+2h^2(3(2+E(-2+\beta))(2+n\beta)\lambda_2^{\,2}+2(36+20n\beta+E(-36))\lambda_2\lambda_3)),$$

$$C[6]=\frac{1}{480(h+\lambda_2)^2(h+\lambda_3)^2}h^2Sc(h(h^2(40+40n\beta+\mathrm{E}(-40+\beta(40+n(-40+33\beta)))))$$
$$+20h(4+3n\beta+\mathrm{E}(-4+\beta(3-3n+2n\beta)))\lambda_2+10(2+\mathrm{E}(-2+\beta))(2+n\beta)\lambda_2^{\,2})+5$$
$$(h^2(24+28n\beta+\mathrm{E}(-24+\beta(28+n(-28+25\beta)))))+4h(12+10n\beta+\mathrm{E}(-12+\beta(10+n(-10+7\beta))))\lambda_2$$
$$+6(2+\mathrm{E}(-2+\beta))(2+n\beta)\lambda_2^{\,2})\lambda_3+60(n+\mathrm{E}(1+n(-1+\beta)))\beta(h+\lambda_2)\lambda_3^{\,2})\xi,$$

$$C[7]=-\frac{h(A_6(h+2\lambda_4)+A_4h^2(h+4\lambda_4)+5\mathrm{E}h^4nPeSc\beta^2(h+\lambda_3)(h+6\lambda_4)\xi)}{1920(h+\lambda_2)^2(h+\lambda_3)^2(h+\lambda_4)},$$

$$C[8]=-\frac{h^2(A_5(h+3\lambda_4)+A_3h^2(h+5\lambda_4))}{1920(h+\lambda_2)^2(h+\lambda_3)^2(h+\lambda_4)^2},$$

$$A_1=-2DahHr^2(h+\lambda_2)(h+\lambda_3)(h+\lambda_4)-a_1(2h^4+2h\lambda_2\lambda_3\lambda_4+2h^3(\lambda_2+\lambda_3+\lambda_4)+DaGr\lambda_1(Rb\lambda_2\lambda_3+Nr\lambda_2\lambda_4-a_3\lambda_3\lambda_4)$$
$$+DaGrh\lambda_1(Rb(\lambda_2+\lambda_3)+Nr(\lambda_2+\lambda_4)-a_3(\lambda_3+\lambda_4))+h^2(DaGr(-a_3+Nr+Rb)\lambda_1+2\lambda_3\lambda_4+2\lambda_2(\lambda_3+\lambda_4))),$$

$$A_2=a_1\lambda_1Da(h+\lambda_2)(h+\lambda_3)(h+\lambda_4),$$

$$A_3=-2PeSc\beta(h+\lambda_3)\xi(8n(h+\lambda_2)+E(8(1+n(-1+\beta))\lambda_2+n\beta(4\lambda_3+3\lambda_4+6\lambda_4\Omega)+h(8+n(-8+15\beta+6\beta\Omega))))),$$

$$A_4=5PeSc(h+\lambda_3)\xi(3(2+E(-2+\beta))(2+n\beta)\lambda_2^{\,2}+2En\beta^2\lambda_3\lambda_4(1+2\Omega)+\beta(E+n-En\beta)\lambda_2(3\lambda_3+2\lambda_4+4\lambda_4\Omega)+h^2(12+8n\beta(2+\Omega)$$
$$+E(-12-8(-1+n)\beta(2+\Omega)+3n\beta^2(5+4\Omega)))+2h(\lambda_2(12+n\beta(11+4\Omega)+E(-12+4n\beta^2(2+\Omega)-(-1+n)\beta(11+4\Omega)))$$
$$+\beta(n(3\lambda_3+2\lambda_4+4\lambda_4\Omega)+E((2-2n+3n\beta)\lambda_4(1+2\Omega)+\lambda_3(3+n(-3+2\beta(2+\Omega)))))))),$$

$$A_5=-20Pe(h+\lambda_2)(2Pe\lambda_2+Sc\lambda_3\xi(2(n+E(1+n(-1+\beta))))\beta\lambda_3\lambda_4(1+2\Omega)+(2+E(-2+\beta))(2+n\beta)\lambda_2(2\lambda_3+\lambda_4+2\lambda_4\Omega))$$
$$+h^3Sc\xi(12+8\Omega+8n\beta(1+\Omega)+E(-8(-1+n)\beta(1+\Omega)-4(3+2\Omega)+n\beta^2(5+6\Omega)))$$
$$+h^2Sc\xi((4+4n\beta+E(-4+\beta(4-4n+3n\beta)))\lambda_4(1+2\Omega)+(2+E(-2+\beta))(2+n\beta)\lambda_2(3+2\Omega)+\lambda_3$$